Meas. Sci. Technol. **10** (1999) 687–696. Printed in the UK PII: S0957-0233(99)01491-5

A micro-electro-mechanical-system-based thermal shear-stress sensor with self-frequency compensation

J B Huang†, F K Jiang‡, Y C Tai‡ and C M Ho§

† David Sarnoff Research Center, Princeton, NJ 08543, USA
‡ Mechanical and Aerospace Engineering Department, University of California, Los Angeles, CA 90095, USA
§ Department of Electrical Engineering, California Institute of Technology, Pasadena, CA 91125, USA

Received 2 February 1999, in final form 29 April 1999, accepted for publication 5 May 1999

Abstract. By applying the micro-electro-mechanical-system (MEMS) fabrication technology, we developed a micro-thermal sensor to measure surface shear stress. The heat transfer from a polysilicon heater depends on the normal velocity gradient and thus provides the surface shear stress. However, the sensitivity of the shear-stress measurements in air is less than desirable due to the low heat capacity of air. A unique feature of this micro-sensor is that the heating element, a film 1 μm thick, is separated from the substrate by a vacuum cavity 2 μm thick. The vacuum cavity prevents the conduction of heat to the substrate and therefore improves the sensitivity by an order of magnitude. Owing to the low thermal inertia of the miniature sensing element, this shear-stress micro-sensor can provide instantaneous measurements of small-scale turbulence. Furthermore, MEMS technology allows us make multiple sensors on a single chip so that we can perform distributed measurements. In this study, we use multiple polysilicon sensor elements to improve the dynamic performance of the sensor itself. It is demonstrated that the frequency-response range of a constant-current sensor can be extended from the order of 100 Hz to 100 kHz.

Keywords: MEMS shear-stress sensor, micro-machine technologies, flow sensing

1. Introduction

A fluid flowing past a solid boundary exerts normal and tangential forces on the surface. Many techniques for measuring the tangential stress have been developed (Winter 1977, Haritonidis 1989, Goldstein 1996). The most direct way of determining the shear stress is to measure the force exerted on a small surface area. By fabricating a floating element that is flush to the surface, the shear stress can be determined from the displacement of the element or from the force required to keep the element in a null position. The MEMS technology has obvious advantages for fabricating a small sensing element and provides an almost point measurement.

A typical sensor consists of a small plate suspended by tethers that is fabricated by surface micromachining techniques (Schmidt *et al* 1988, Shajii *et al* 1992). As fluid flows over the plate, the surface shear force causes an in-plane deflection of the plate, which can be measured by a strain gauge deposited on the tethers. By placing electrodes on the plate, the motion of the plate can be made to produce changes in capacitance that can be used as a sensing output (Pan *et al* 1994, Mehregany and Bang 1995). The displacement of the plate can also be measured by using optical means (Padmanabhan *et al* 1995). Since these techniques require that a portion of the wall be allowed to move in a direction parallel to the boundary, the sensing plate must have a gap around its perimeter. A consequence of this necessary feature is that the unit can be contaminated by dust and moisture from the ambient.

The surface shear stress can be related to the strain rate of the flow at the boundary. For example, the wall shear stress along the streamwise direction of a Newtonian fluid is

$$\tau = \mu \left.\frac{\partial U}{\partial y}\right|_{y=0}$$

where U is the streamwise velocity, y is the direction normal to the surface and μ is the viscosity. Many methods of measuring the wall shear stress are based on this relationship. One obvious method is to obtain the slope at the wall by differentiating the velocity profile. The challenge is to acquire an accurate near-wall velocity distribution. When a hot wire is placed very close to the wall, the surface affects

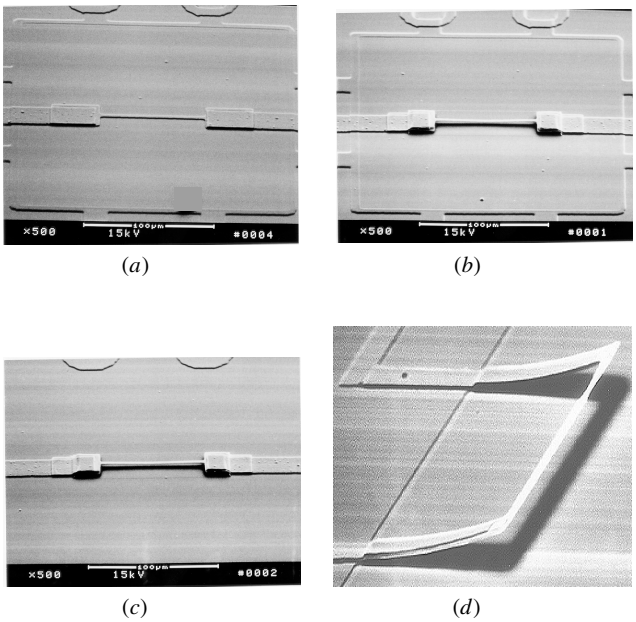

Figure 1. SEM pictures of four kinds of shear-stress micro-sensors. (*a*) Type I sensor, (*b*) type II sensor, (*c*) type III sensor and (*d*) type IV sensor.

the heat transfer and an erroneous reading will result unless corrections are made. The noise level of optical velocimetry, such as is obtained from a laser Doppler velocimeter or a particle-image velocimeter, is mostly due to the reflection from the wall. The wall also influences the trajectories of particles seeded in the flow.

The Preston tube (Preston 1953) is one of the most commonly used instruments for measuring the time-averaged wall stress. It is a fairly simple device and it is easy to use. The Preston tube is a small, rectangular, total-head tube that uses the wall as one side of the tube. The pressure reading is related to the dynamic head near the wall. If the tube is small enough to be immersed in the region where $\tau = \mu(U/y)$, a simple relationship between the measured pressure and the time-averaged shear stress can be established (Goldstein 1996).

The Stanton gauge is another commonly used instrument for measuring time-averaged shear stress. The Stanton gauge is formed by placing a thin razor blade above a static pressure hole. The difference between the pressure readings with and without the blade can then be related to the time-averaged surface shear stress (Stanton *et al* 1920).

The rate of heat transfer from small thermal elements mounted flush on the surface can be related to the local surface shear stress. The thermal method for shear-stress measurement is an indirect but extensively used technique due to its simple configuration. A metal (e.g. platinum or tungsten) is traditionally used as the heating element. When a heating current passes through the heating element, the change in voltage across the element can be correlated to the shear stress. One disadvantage of using the thermal shear-stress probes is the loss of heat to the substrate, which reduces the sensitivity. This problem become a critical one when the probe is operated in air, since air itself has a low heat capacity. Therefore, the thermal shear-stress measurement in air usually has a low signal-to-noise ratio.

By applying the MEMS technology that emerged during the late 1980s, we can alleviate loss by conduction of heat from the substrate and improve the performance of the thermal shear-stress sensor (Liu *et al* 1994, Jiang *et al* 1995, 1996, Huang *et al* 1995a, b, 1996). The MEMS fabrication technique utilizes lithography to expose the deposited photo-resist patterns on the chip and the unwanted part is then selectively removed by etchants. By repeating the deposition–removal processes, sensors and actuators with intricate geometry can be produced (Ho and Tai 1996, 1998). Using surface micromachining, we fabricated a vacuum chamber 2 μm thick under the diaphragm that supports the heating element. This vacuum chamber will substantially reduce the transfer of heat to the substrate and therefore the sensitivity will be increased.

In this paper, we will first present the manufacturing process. Then, the static and dynamic calibrations are discussed. Finally, the idea of self-frequency compensation for increasing the dynamic response will be introduced.

2. Sensor design and the fabrication process

Four different configurations of the shear-stress micro-sensor have been designed and fabricated (figure 1). The sensing element is made of polysilicon resistors. For type I, the resistor rests on the silicon nitride diaphragm, which has a vacuum chamber below it. The size of the vacuum cavity is 200 μm × 200 μm × 2 μm. Type II has a similar configuration except that the polysilicon resistor is raised 3–5 μm above the diaphragm by a bridge structure on the diaphragm. Type III is similar to type II except the polysilicon resistor is elevated above a solid substrate. The polysilicon resistor of the type IV sensor is supported by two long arms that are placed on a solid substrate. This resistor is 3 μm wide and has several different lengths. Metal leads connect the sensor element to the printed circuit (PC) boards through bonding pads. A traditional hot-film sensor structure sits directly on the substrate; it is also made on the same chip for the purpose of comparison.

The major processing steps (Jiang *et al* 1995) for the type I sensor are schematically shown in figure 2. First, a 200 nm layer of silicon nitride is deposited on a 4 in^2 wafer by LPCVD and patterned to define the diaphragms (as 200 μm × 200 μm windows in the nitride layer). Exposed silicon substrate is etched down 600 nm by a wet silicon etchant and then a thick wet oxide ($\simeq$1.1 μm) is grown, both for planarization and to provide a sacrificial layer. Next, a 500 nm layer of phosphosilicate glass (PSG) is deposited by LPCVD at 450 °C and patterned (figure 2(*a*)). A blank low-stress silicon nitride ($\simeq$1.0 μm) is then deposited by LPCVD as the diaphragm material (figure 2(*b*)). Then, etching holes are opened in the silicon nitride layer to expose the sacrificial PSG which, together with the underlying thermal oxide, is etched away by highly concentrated hydrofluoric acid (HF) (49 wt%) to form the cavity underneath the diaphragm (figure 2(*c*)). The wafer is then dried and a 400 nm layer of silicon nitride is deposited at a vacuum pressure of 300 mTorr to seal the cavity and to form the vacuum chamber (figure 2(*d*)). To form the sensor resistors, a 450 nm layer of polysilicon is deposited by LPCVD and then patterned using a SF_6 plasma (figure 2(*d*)). Doping by ion implantation

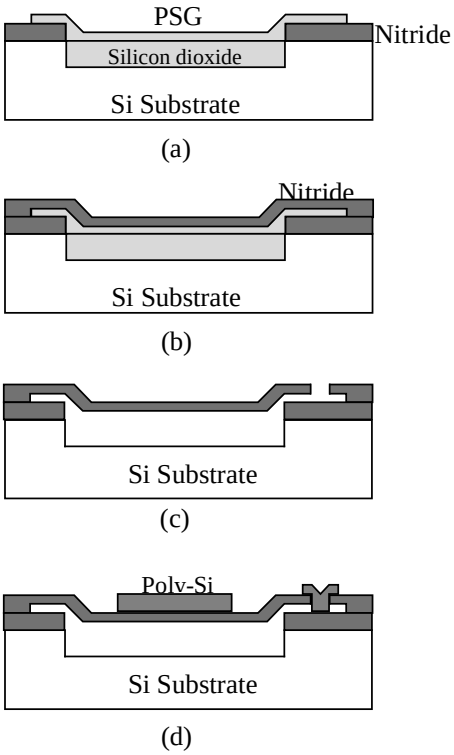

Figure 2. The major steps for fabricating the micro-sensor (type I is shown).

follows. Two phosphorous-doping dose levels have been chosen, namely 10^{16} and the 10^{14} cm^{-2}. The wafer is then annealed at 1000 °C for 1 h to activate the dopant and to reduce the intrinsic stress in the polysilicon. A 100 nm thick layer of nitride is deposited by LPCVD as protection for the polysilicon resistors. Finally aluminium metallization forms the leads and the annealing of aluminium in N_2 at 420 °C for 30 min completes the process. For the other three types of sensors, an additional sacrificial layer is added to form the bridge structure.

The measured temperature coefficient of resistivity (TCR) of the sensor resistor is typically 0.1% °C^{-1} for the higher doping level and −0.25% °C^{-1} for the lower doping level. The sensors in our experiments have the former level unless noted otherwise.

3. Sensor operation and calibration

3.1. Sensor operation

The convective transfer of heat from the heated sensor to the ambient fluid is a function of the velocity. When the sensor is placed on a surface where the velocity equals zero, the heat convection is related to the first derivative of the velocity, which is the shear stress generated by the flow. The heating power for the sensor and the wall shear stress, τ, follow the relation (Haritonidis 1989)

$$P = (T - T_0)(A + B\tau^{1/3}) \tag{1}$$

where T_0 is the temperature of the ambient flow and T is the sensor temperature, P is the heating power for the sensor

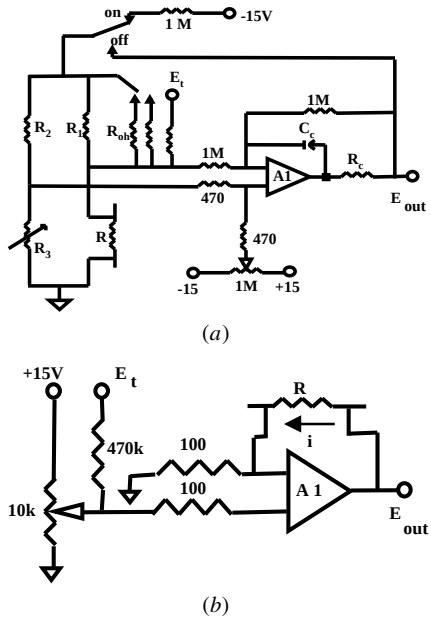

Figure 3. The circuit diagrams of (*a*) CT and (*b*) CC modes of operation.

to compensate for the heat convection and A and B are calibration constants. We can operate the sensor in constant temperature (CT) or constant current (CC) mode. For the CT mode, the sensor resistance, R, is kept constant by a feedback circuit and $P = E^2/R$, where E is the voltage across the sensor. Equation (1) becomes

$$E^2 = (A_T + B_T\tau^{1/3}). \tag{2}$$

For the CC mode, the current passing through the sensor is a constant and $P = EI$. From equation (2),

$$E = (A_C + B_C\tau^{1/3}). \tag{3}$$

The sensing element is made of polysilicon, which has a wide range of resistance that can be adjusted by changing the doping level of the phosphorus. This is a very useful property, because the frequency response of the hot film is a function of the sensor resistance. We found that the optimum resistance range of the micromachined sensor is 1–10 kΩ, which is much higher than that of the traditional metal sensor (5–50 Ω). This is the main reason why our shear-stress micro-sensor achieves such a high frequency response. On the other hand, the characteristics of the operational amplifier limit the maximum probe resistance which can be used in the bias circuit. The CT and CC anemometer circuits used in the experiment are shown in figure 3. The resistance of the sensing element, R, can be approximately related to its temperature, T, by the linear equation

$$R = R_0[1 + \alpha(T - T_0)] \tag{4}$$

where R_0 is the average resistance at a reference temperature, T_0, and α is the TCR of the sensor. This TCR is an additional adjustable parameter of a polysilicon sensor. It can take either positive or negative values according to the phosphorus content. By using this property, we can develop a self-compensation technique that can further extend the range of

frequency response. A parameter governing the operation of a hot-film sensor is the overheat ratio defined as (Blackwelder 1981)

$$a_T = (T - T_0)/T_0. \tag{5}$$

During operation, it is more practical to use a resistive overheat ratio defined by

$$a_R = (R - R_0)/R_0 = \alpha(T - T_0). \tag{6}$$

The relationship between the two overheat ratios is

$$a_R = (\alpha T_0) a_T. \tag{7}$$

It should be noted that the resistive overheat ratio, a_R, could be either positive or negative depending on the sign of the TCR, α, but the temperature overheat ratio, a_T, is always positive.

3.2. Sensor calibration

The shear-stress sensor was calibrated in a two-dimensional (2D) channel flow facility. The channel is 4.88 m long with a cross section of 0.61 m × 0.025 m. The air flow is provided by an axial blower driven by a dc power supply. The settling chamber has a honeycomb and screens for reducing the turbulence level. A 10:1 contraction leads the flow into a 2D test section. The velocity ranges from 5 to 30 m s^{-1}. The flow at the entrance of the test section is laminar and becomes transitional and eventually reaches fully developed channel flow.

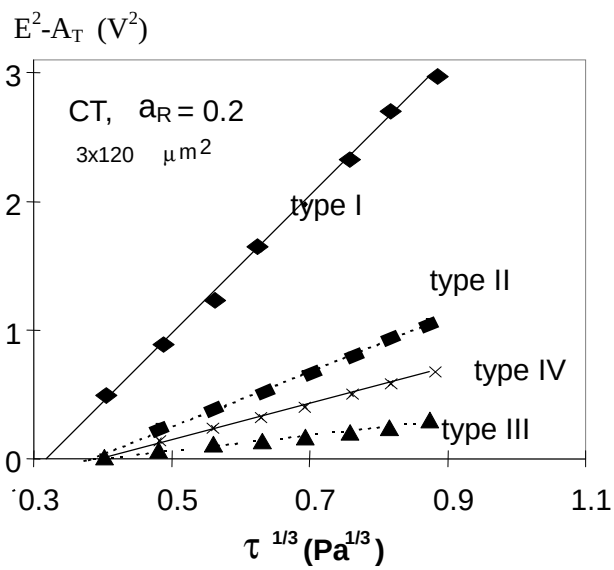

Figure 4. The calibration results for the four types of sensor operated in CT mode.

For sensitivity calibration, we adapted two methods. In a fully developed channel flow, the surface shear stress, τ, is linearly proportional to the streamwise pressure gradient:

$$\tau = \frac{h}{2}\frac{\Delta P}{L_s}. \tag{8}$$

where h is the channel height and ΔP is the pressure drop over the streamwise length L_s.

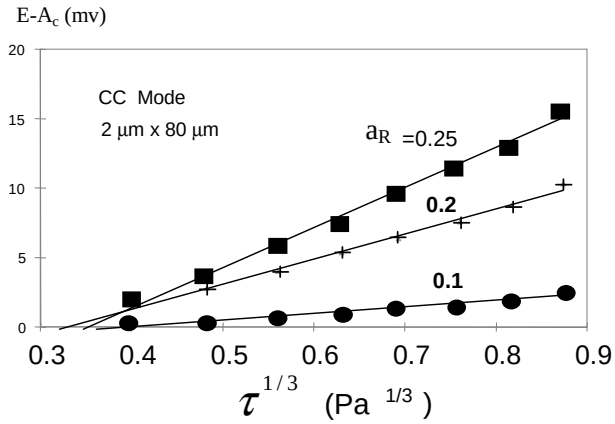

Figure 5. The calibration results for a CC sensor operated at $a_R = 0.25$, 0.2 and 0.1.

In the second method, an empirical relationship between the Reynolds number and the wall shear stress for channel flow was developed (Laufer 1951) as

$$\frac{U_\tau}{U_0} = 0.108 Re^{-0.089} \tag{9}$$

where U_τ is the shear velocity equalling $(\tau/\rho)^{1/2}$, U_0 is the free-stream velocity, Re is the Reynolds number based on the free-stream velocity and half height of the wind tunnel and ρ is the density of air. This calibration method is simple since we need only measure the free-stream speed and do not need to know the pressure gradient.

The calibration results for four types of shear-stress sensors are shown in figure 4. These sensors are operated in the CT mode with a resistive overheat ratio of 0.2. The sensor elements all have the same dimensions of 3 μm × 120 μm.

As expected, the type I sensor has the best sensitivity. When the output of a type I sensor was compared with that of the sensor element placed directly on the substrate without a vacuum chamber (Huang *et al* 1995b), the sensitivity was an order of magnitude higher. The sensitivity is a function of the area heated. Part of the film of a type I sensor is heated due to the direct contact of the sensing element and functions as part of the sensor. Therefore, the type I sensor is more sensitive than the type II sensor. The type II sensor is much more sensitive than the type III sensor. Since the type IV sensor has longer supporting arms than those of the type III sensor, the arms separate the hot sensing element further from the heat sink (i.e. the substrate). Therefore, the type IV sensor has better sensitivity. Overall, the type I sensor has the best performance and was therefore studied and is reported on in the following sections.

The calibration results for the type I sensor (2 μm × 80 μm) operated in the CC mode and with initial resistive overheat ratios of 0.25, 0.2 and 0.1 are shown in figure 5. It can be seen that the higher the overheat ratio the higher the sensitivity. This is because the temperature difference between the air and the sensors is larger, ranging from 0.1 to 0.25 for the highly phosphorus-doped polysilicon sensor and from −0.25 to −0.5 for the low phosphorus-doping level. Within these ranges of overheat ratios, the temperature differences between the heated sensor and the ambient air are

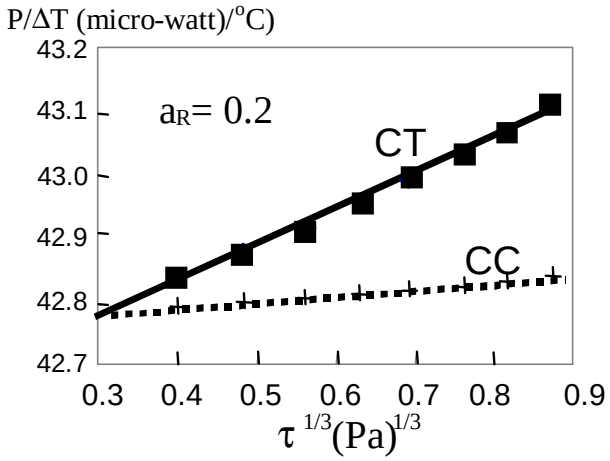

Figure 6. A type I sensor with dimensions 2 μm × 80 μm operated in CT and CC modes.

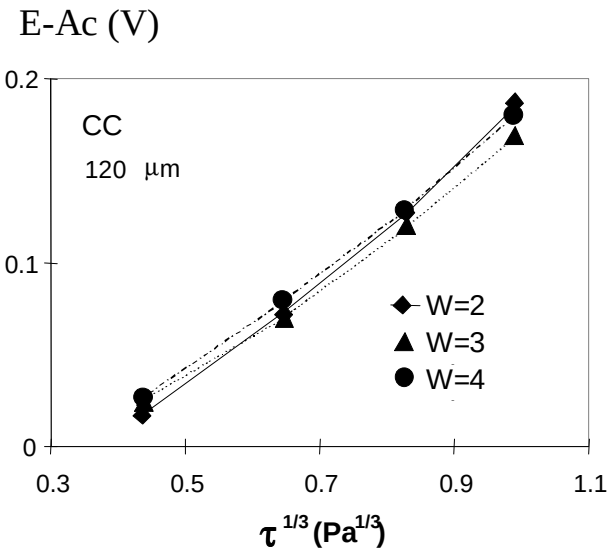

(*a*)

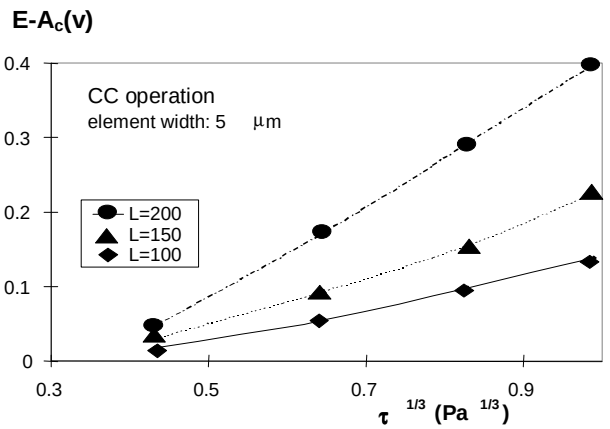

(*b*)

Figure 7. Sensitivities of sensors with various (*a*) widths and (*b*) lengths.

approximately less than 200 °C. The polysilicon sensor has stable material properties for temperatures below this level. It can be seen that for a sensor operated at the same overheat ratio, the CT mode has a higher sensitivity than that of the CC mode (figure 6).

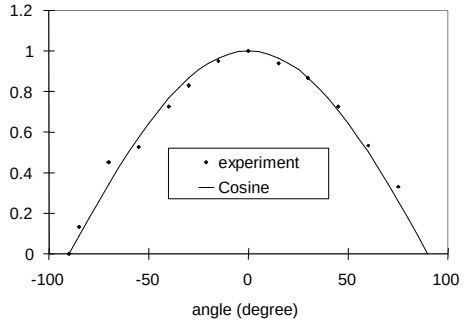

Figure 8. The directional sensitivity of a sensor.

The effects of the sensor dimensions on their sensitivities have been measured and the results are shown in figure 7. The sensors utilized have a phosphorus-doping level in the negative ranges of the TCR and resistive overheat ratio. The resistive overheat ratio tested in figure 7 is -0.5. Figure 7(*a*) shows data for sensors with the same length (120 μm) but with widths of 2, 3 and 4 μm. The data show that the width has a minor effect on the sensitivity. A sensor with a large width, 5 μm, was tested. L/D in this test case (figure 7) was only 20–40 and the temperature distribution along the sensor is not uniform. The sensitivity becomes length dependent (figure 7(*b*)).

The directional dependence of the sensitivity was checked (figure 8). The flow direction normal to the sensor element is defined as 0° and the flow direction parallel to the length is defined as ±90°. The data follow a cosine function. We can use the directional dependence to obtain the shear stress in two directions simultaneously by the combination of the outputs of two inclined sensors.

3.3. Temperature compensation

At a constant free-stream velocity, i.e. constant shear stress, the output of the shear-stress sensor is sensitive to the ambient temperature. This is the result of the doping level, which is chosen for high shear-stress sensitivity. Both for CC and for CT operation, the temperature effect (figures 9(*a*) and (*b*)) depends on the overheat ratio.

We can compensate for the temperature sensitivity either by using a signal-processing software package or by using hardware circuitry. Here, we develop a circuit (figure 10) that uses another on-chip polysilicon sensor to accomplish the temperature compensation. This sensor has a TCR matched with that of the shear-stress sensor but is operated at an overheat ratio less than 0.01, so that it functions as a temperature sensor. The output of op-amp A3 is therefore a function of the ambient temperature and fed into op-amp A2 to compensate for the temperature dependence of the shear-stress sensor.

The results with and without temperature compensation for a CT shear-stress sensor operated at a resistive overheat ratio of 0.1 are shown in figure 11. The temperature dependence decreases from 47 to 1 mV °C^{-1}. This circuit provides an instantaneously temperature-compensated shear-stress signal. Furthermore, the output of one temperature

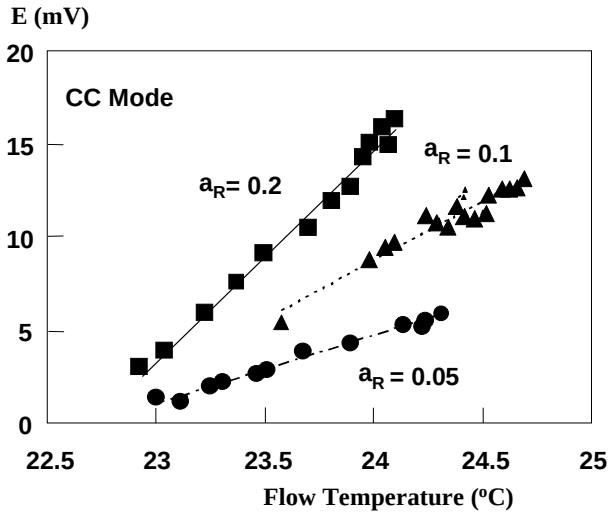

(*a*)

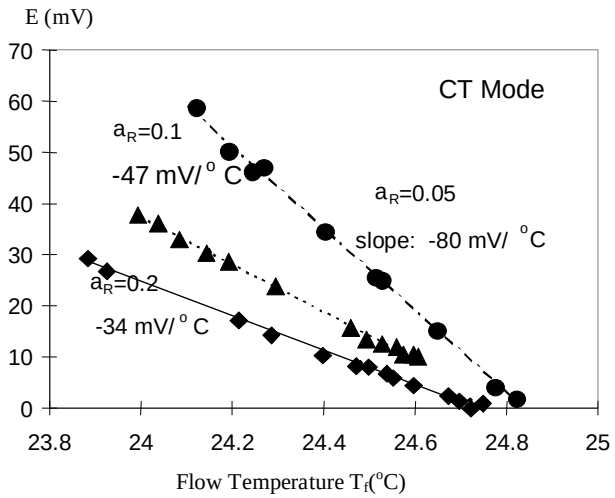

(*b*)

Figure 9. The temperature effect of the sensor at various overheat ratios for (*a*) CC and (*b*) CT operation.

sensor can be used to compensate multi-channel shear-stress sensors. This temperature-compensation technique is also suitable for CC operation.

4. The frequency response and self-frequency compensation

4.1. Time constants of a surface thermal sensor with a heat-insulation layer

The dynamic response of the micro-sensor is studied according to the model shown in figure 12(*a*). The sensor element is at the top of the insulation layer (a silicon nitride diaphragm) and the cavity is underneath the insulation layer. We limit this analysis to the case of sensing elements with large length-to-width ratios, for which the end heat loss is small and can be neglected. The silicon substrate with a large thermal conductivity is treated as a heat sink. In figure 12, the q with subscripts s, i and c represent, respectively, the conductive transfer of heat from the sensor to the insulation layer, lateral conduction inside the insulation layer and the convective transfer of heat to the fluid. The same subscripts are used for other thermal parameters.

The energy-balance equations of figure 12(*a*) are

$$i^2R = h(u_\tau)A(T - T_0) + c_s m_s \frac{\mathrm{d}T}{\mathrm{d}t} + q_s \tag{10}$$

$$q_s = q_1 + c_i m_i \frac{\mathrm{d}T_i}{\mathrm{d}t}. \tag{11}$$

The heating current, I, through the resistive sensor, R, produces the heating power $p = i^2R$. The power is balanced by three processes. The first is the convective transfer of heat, $q_c = h(u_\tau)A(T - T_0)$, to the sensor's environment, in which T and T_0 are the temperatures of, respectively, the sensor element and the ambient fluid. The convective-heat-transfer coefficient is represented by $h(u_\tau)$ and it is a function of the shear velocity, u_τ. The relationship between u_τ and the wall shear stress, τ, is $\tau = u_\tau^2\rho$, where ρ is the fluid density. A is the wetted area of the sensor, $A = WL$, where W and L denote the width and length. The second process involves

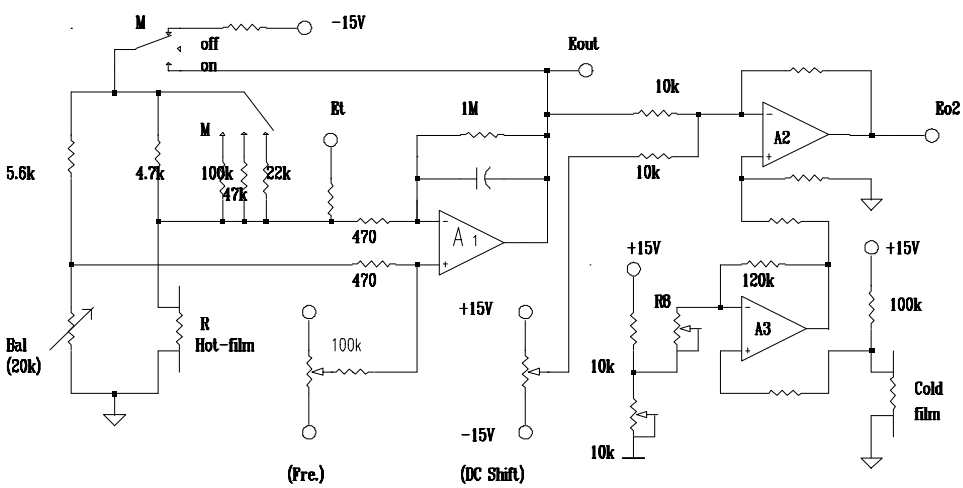

Figure 10. The temperature-compensation circuit for CT operation of the sensor.

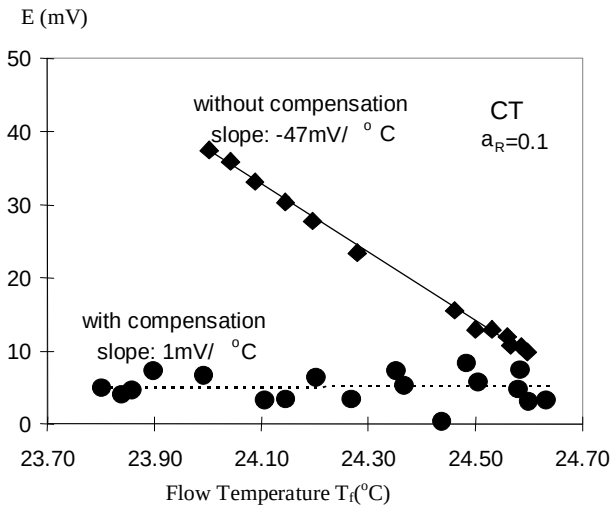

Figure 11. The temperature-compensation results for the sensor at an overheat ratio of 0.1 and in CT mode.

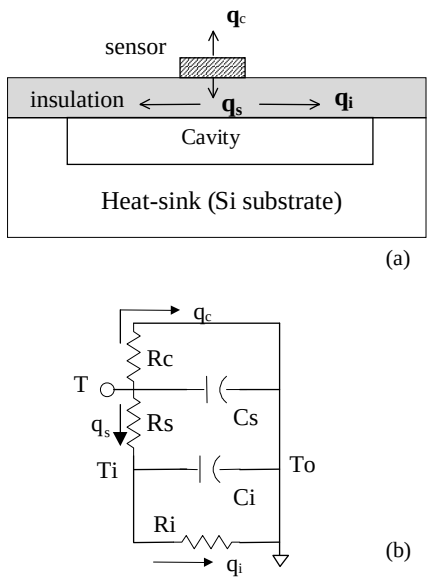

Figure 12. The heat-transfer models for (*a*) the general sensor with a cavity underneath and (*b*) the electrical analogy's equivalent circuit.

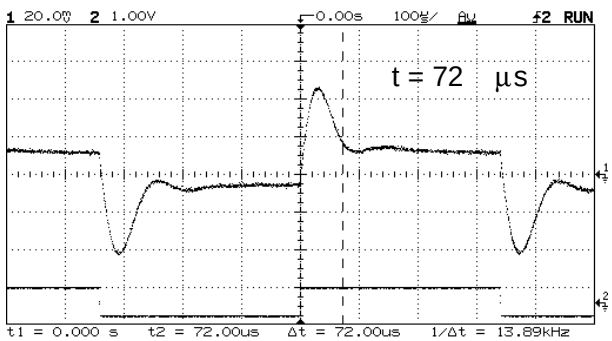

Figure 13. A typical square-wave response of the hot-film sensor in the CT mode. The size of the sensor is 2 μm × 80 μm and the overheat ratio is 0.12.

the energy stored in the sensor element, $c_s m_s(\mathrm{d}T/\mathrm{d}t)$, in which c_s, m_s and T are, respectively, the specific heat, mass and temperature. The third process is conductive transfer of heat from the sensor to the insulation layer, q_s, which comprises two terms, as shown in equation (11). One is the energy stored in the insulation layer, $c_i m_i(\mathrm{d}T_i/\mathrm{d}t)$; the other is q_i, the conductive transfer of heat laterally from the insulator to the silicon substrate. The electrical analogy's equivalent circuit of the energy-balance equation is shown in figure 12(*b*). The two conductive-heat-transfer terms can be described as follows:

$$q_s = \frac{k_s A(T - T_i)}{d_s} \tag{12}$$

$$q_i = \frac{2k_i d_i L(T_i - T_0)}{L_c} \tag{13}$$

where k_i and k_s are the thermal conductivities of, respectively, the insulation and the sensor element; and L_c is the half length of the cavity side. The '2' in equation (13) is a result of the bi-directionality of heat transfer in the insulation layer.

By combining equations (10)–(13), considering the small fluctuating variables, neglecting higher order terms and using a Laplace transform, the transfer function for the relationship between the sensor's temperature and the input variable, ΔF, can be obtained as

$$\frac{\Delta T}{\Delta F} = \left(\frac{a_R}{\alpha i^2 R_0}\right) \frac{t_2 s + 1}{t_1 t_2 s^2 + (t_1 + t_2 t_3)s + 1} \tag{14}$$

$$\Delta F = \frac{\partial P}{\partial i}\Delta I - (\bar{T} - T_0)A\Delta H \tag{15}$$

where ΔF is the Laplace-transform form of the input variable (which is a function both of the perturbation of the electrical current input ΔI, and of the shear-stress-related perturbation of the input, ΔH) and $\bar{T}$ is the static temperature of the sensor. In equation (14), a_R, α and R_0 are, respectively, the resistive overheat ratio, the temperature coefficient of resistivity (TCR) ($1\,^\circ\mathrm{C}^{-1}$) of the sensor element and the sensor resistance at temperature T_0. The time constants t_1, t_2 and t_3 (in equation (14)) are

$$t_1 = \frac{a_R}{\alpha i^2 R_0} c_s m_s$$

$$t_2 = \frac{d_s}{k_s A} c_i m_i \tag{16}$$

$$t_3 = \frac{a_R}{\alpha i^2 R_0} c_i m_i.$$

Although the system shown in equation (14) is of second order, the pole $s_1 \approx -1/(t_1+t_2+t_3)$ is dominant, so the system behaves just like a first-order system with a time constant of

$$t_c = t_1 + t_2 + t_3. \tag{17}$$

This total time constant comprises three parts: t_1 is exactly the same as the time constant found previously (Blackwelder 1981); the other two parts, t_2 and t_3, obtained here indicate how the insulation-layer parameters affect the sensor's dynamic performance. The time constant of a sensor operated in CC mode (figure 9 in the paper by Liu *et al*

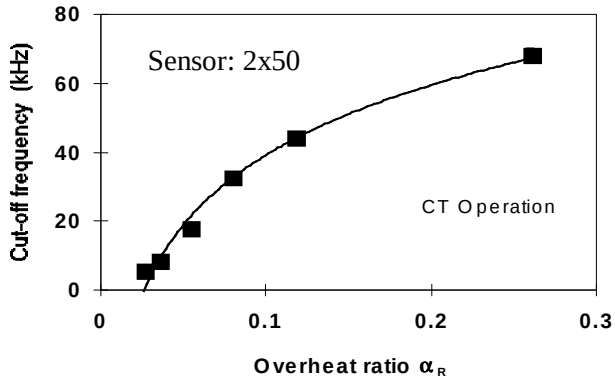

Figure 14. The cut-off frequency of the micro-sensor versus the resistive overheat ratio in CT mode.

(1994)) was measured and found to equal 350 μs. The calculated values of the various time constants are $t_1 = 49\,\mu$s, $t_2 = 0.1\,\mu$s and $t_3 = 293\,\mu$s. The value of t_c is 342 μs, which is in good agreement with the measured value. From equations (16) and (17), it can be seen that the existence of the insulation layer tends to increase the time constant. The smaller the thermal conductivity, k_i, of the insulation layer the larger the effect. The larger the specific heat, c_i, and mass, m_i, of the insulation layer the larger the time constant (Huang *et al* 1996).

4.2. Frequency responses of sensors with positive TCRs

Since well-defined, high-frequency, shear-stress fluctuations for calibrating the frequency response of the sensor are not readily available, electronic test signals are usually used to determine the time constant of the system. According both to theoretical analyses and to experimental confirmation (Freymuth 1977, Reda 1991, Albin *et al* 1993, Moen and Schneider 1993), the frequency response can be obtained by feeding sine waves or square waves into the sensor driver circuit. The terminal, E_t, in figure 3 is for this purpose.

A polysilicon sensor doped with the higher level of phosphorus with a typical sheet resistance of 50 Ω per square has a positive TCR. The measured frequency response of a $2\,\mu\text{m} \times 80\,\mu\text{m}$ micro-sensor in the CC mode is 500 Hz. Much better dynamic performance can be obtained by operating the sensor in the CT mode. The square-wave response of the sensor is shown in figure 13, in which the lower wave is the input and the upper wave is the response output. The time constant is 72 μs. A higher frequency response can be obtained by increasing the overheat ratio of the sensor or by using a smaller sensor. Figure 14 presents the cut-off frequency versus the resistive overheat ratio. At $a_R = 0.25$, the frequency response of a sensor of size $2\,\mu\text{m} \times 50\,\mu\text{m}$ can reach 70 kHz.

4.3. Frequency responses of sensors with negative TCRs

Most thermal sensors with positive TCRs exhibit low-pass-filter characteristics due to the thermal lag. When a sensor element is doped with a low level (with a typical sheet resistance of 21 kΩ per square) of phosphorus, its TCR is negative. The frequency response behaves like that of a high-pass filter (figure 15).

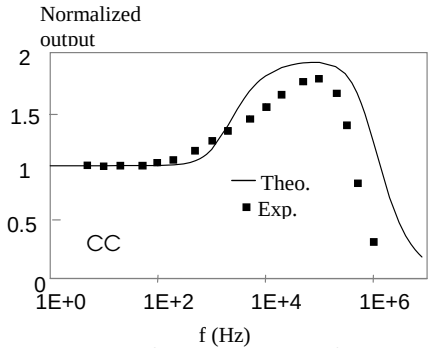

Figure 15. The frequency response of a sensor with a negative TCR.

We use a CC shear-stress sensor to examine this feature; the energy balance equation for the sensor element can be written as (Blackwelder 1981)

$$c_s m_s \frac{\mathrm{d}T}{\mathrm{d}t} = i^2 R - F(\tau, T) \tag{18}$$

where c_s, m_s and T represent, respectively, the specific heat, mass and temperature of the sensor, i^2R is the power input and F is the heat convected from the sensor to the ambient. On using the Taylor expansion to look into the response to electrical perturbations and neglecting higher order terms, the equation governing the dynamic response of the sensor element follows as

$$M_1 \frac{\mathrm{d}\Delta T}{\mathrm{d}t} + \Delta T = F'(t) \tag{19}$$

where

$$M_1 = \frac{c_s m_s}{\alpha R_0} \frac{a_R}{i^2}.$$

$$F'(t) = \frac{2a_R}{\alpha}(1 + a_R)\frac{\Delta i}{i}. \tag{20}$$

By taking the Laplace transform of equation (19), the change in transfer function for the relationship between the electrical current, Δi, and the sensor temperature, ΔT, can be derived as

$$\frac{\Delta T}{\Delta i} = \frac{F'(t)}{1 + M_1 s}. \tag{21}$$

For the CC circuit (figure 3), the relation between the output voltage, E_{out}, and the input current, i, can be described by

$$M_s \frac{\mathrm{d}E_{out}}{\mathrm{d}t} + E_{out} = iR \tag{22}$$

where M_2 is the time constant for the circuit. Similarly, by considering the fluctuating parts, taking the Laplace transform of equation (22) and combining it with equation (21), we can get the transfer function for the system

$$\frac{\Delta E_{out}}{\Delta i} = \frac{R}{\left(1 + \mathrm{j}\frac{\omega}{\omega_2}\right)}\left(\frac{2a_R(1 + a_R)}{1 + \mathrm{j}\frac{\omega}{\omega_i}} + 1\right) \tag{23}$$

where $\omega = 2\pi f$ is the frequency, $\omega_1 = 1/M_1$ and $\omega_2 = 1/M_2$ are the corner frequencies for, respectively, the sensor

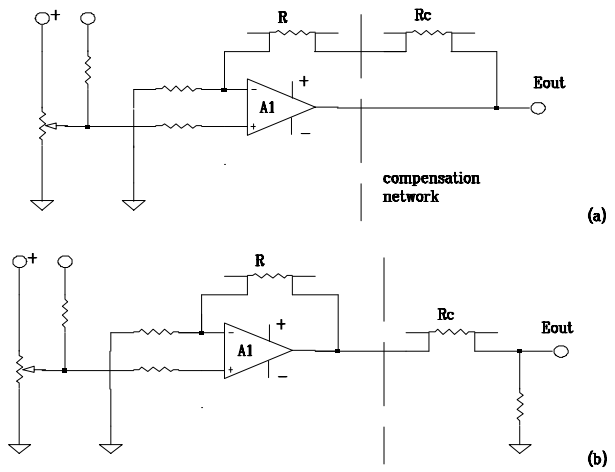

Figure 16. The schematic diagrams of the self-compensation network.

and the circuit. The amplitude of the transfer function can be derived as

$$\left|\frac{\Delta E_{out}}{\Delta i}\right| = \frac{R}{[1+(\omega/\omega_2)^2]^{1/2}}\frac{2a_{R_R}(1+a_{R_R})}{[1+(\omega/\omega_1)^2]^{1/2}}. \qquad (24)$$

The theoretical curve (equation (24)) is shown in figure 15. For $\omega_1 < \omega < \omega_2$, the above equation can be simplified to

$$\left|\frac{\Delta E_{out}}{\Delta i}\right| = R\left(\frac{2a_R(1+a_R)}{\omega/\omega_1}+1\right). \qquad (25)$$

The TCR, α, of the sensor is negative and hence the resistive overheat ratio, a_R, is also negative. Therefore, the above equation shows that the amplitude of the transfer function increases with frequency, since the first term on the right-hand side of the equation is negative. Thus, a sensor with a negative TCR has a high-pass-filter characteristic.

4.4. Self-frequency compensation

By taking advantage of the high-pass-filter characteristics of a negative TCR sensor, a unique self-frequency-compensation technique is illustrated here. We specifically use the CC mode to demonstrate the effectiveness of this concept, because a typical CC sensor has a low frequency response in the range of hundreds of hertz. Lithography allows us to fabricate sensors with different chosen TCR values on a single chip. We use a pair of polysilicon sensors in a CC circuit: one with a positive TCR, R, and the other one with a negative TCR, Rc (figure 16(*a*)). This is the experimental result obtained from a sensor with and without the compensation. By using this technique, the frequency response of a CC sensor can be extended by three orders of magnitude (figure 17(*a*)).

Another frequency compensation, which is similar to an R–C (resistor–capacitor) compensation circuit (discussed above) is realized in figure 16(*b*), in which both the measurement sensor, of resistance R, and in the compensation sensor, of resistance R_c, are of positive-TCR type. This is similar to a differential circuit composed of a capacitor and a resistor. A compensation circuit with differential characteristics can be formed without making any

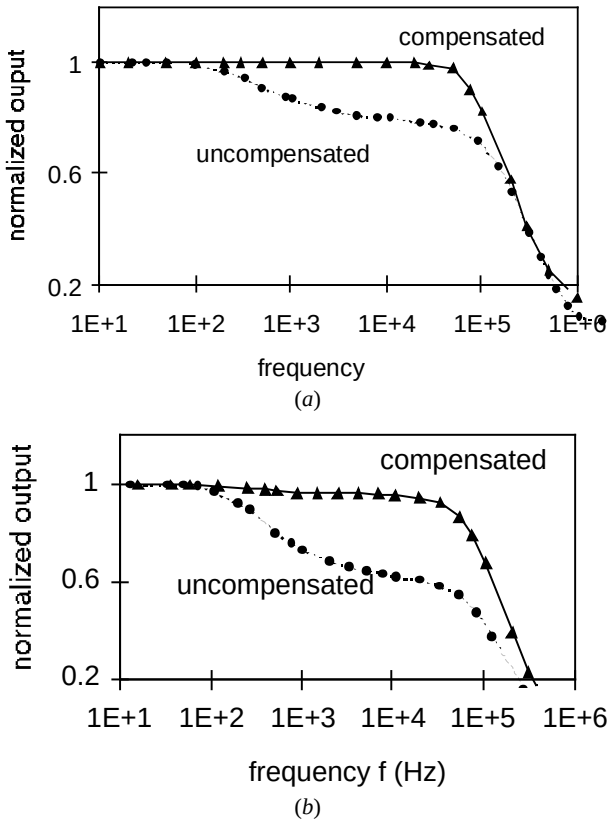

Figure 17. The uncompensated and compensated frequency responses: (*a*) using the circuit of figure 16(*a*) and (*b*) using the circuit of figure 16(*b*). $a_R = -0.7$.

adjustments. With this type of compensation, the frequency response of a typical CC shear-stress micro-sensor can be extended from 500 Hz to about 100 kHz (figure 17(*b*)).

5. Conclusions

Hot-film shear-stress sensors of four types have been designed and fabricated by micro-machining technology. The micro-vacuum chamber substantially reduces the substrate heat conduction and increases the sensor sensitivity. Experimental results show that the shear-stress micro-sensor operating in the constant-temperature mode can reach a cut-off frequency of 70 kHz and a high shear-stress sensitivity. The constant-current shear-stress sensor has a frequency response of only of the order of 100 Hz. When we use a pair of polysilicon elements, one as a shear-stress sensor and one as a compensation element, the frequency response for operation in the CC mode can be increased to the 100 kHz range.

Acknowledgment

This work is supported by an AFOSR-URI contract.

References

Albin S, Bulusu A, Martinson S D and Gray D S 1993 Frequency response simulations of a diamond based sensor for supersonic flows *Proc. ASME Thermal Anenometry*

(Washington, DC) ed D E Stock *et al* (New York: ASME) **ASME-FED 167** pp 181–84
Blackwelder R F 1981 Hot-wire and hot-film anemometers *Methods of Experimental Physics: Fluid Dynamics* ed R J Emrich (New York: Academic) pp 259–314
Freymuth P 1977 Frequency response and electronic testing for constant-temperature hot-wire anemometers *J. Phys. E: Sci. Instrum.* **10** 705–10
Goldstein R J 1996 *Fluid Mechanics Measurements* (London: Taylor and Francis)
Haritonidis J H 1989 The measurement of wall shear stress *Advances in Fluid Mechanics Measurements* ed M Gad-el-Hak (Berlin: Springer) pp 229–61
Ho C M and Tai Y C 1996 MEMS and its applications for flow control *J. Fluids Engng.* **118** 437–47
——1998 Micro-electro-mechanical-systems and fluid flows *Ann. Rev. Fluid Mech.* **30** 579–612
Huang J B, Ho C M, Tung S, Liu C and Tai Y C 1995b Micro thermal shear stress sensor with and without cavity underneath *IEEE Proc. Instruments Measurement Technology Conf. (IMTC/95)* pp 171–4
Huang J B, Liu C, Jiang F, Tung S, Tai Y C and Ho C M 1995a Fluidic shear-stress measurement using surface micromachined sensors *Proc. IEEE Region 10 Int. Conf. Microelectronics and VLSI, Hong Kong* pp 16–19
Huang J B, Tung S, Ho C M, Liu C and Tai T C 1996 Improved micro thermal shear-stress sensor *IEEE Trans. Instrum. Meas.* **45** 570–4
Jiang F, Tai Y C, Huang J B and Ho C M 1995 Polysilicon structures for shear stress sensors *Proc. IEEE Region 10 Int. Conf. Microelectronics and VLSI, Hong Kong* pp 12–15
Jiang F, Tai Y C, Gupta B, Goodman R, Tung S, Huang J and Ho C M 1996 A surface-micromachined shear-stress imager *Proc. IEEE Micro Electro Mechanical Systems Meeting, San Diego, CA* pp 110–15
Laufer J 1951 Investigation of turbulent flow in a two-dimensional channel *NACA report* 1053
Liu C, Tai Y C, Huang J and Ho C M 1994 Surface-micromachined thermal shear stress sensor *Application of Microfabrication to Fluid Mechanics ASME-FED* **197** 9–16
Mehregany M and Bang C 1995 MEMS for smart structures *Proc. Smart Structures and Materials* pp 105–14
Moen M J and Schneider S P 1993 The effect of sensor size and substrate properties on the performance of flush-mounted hot-film sensors *ASME Thermal Anemometry-1993* ed D E Stock *et al* pp 249–61
Padmanabhan A, Goldberg H D, Breuer K S and Schmidt M A 1995 A silicon micromachined floating-element shear-stress sensor with optical position sensing by photodiodes *Digest of Technical Papers, TRANSDUCERS '95, Stockholm* pp 436–9
Pan T, Hyman D, Mehregany M, Reshotko E and Willis B 1994 Calibration of microfabricated shear stress sensors *Digest of Technical Papers, TRANSDUCERS '95, Stockholm* pp 443–6
Preston J H 1953 The determination of turbulent skin friction by means of pitot tubes *J. R. Aeronaut. Soc.* **58** 109–21
Reda D 1991 Rise-time response of nickel-foil-on-Kapton-substrate, hot-film shear stress sensors AIAA paper 91-0169
Schmidt M A, Howe R T, Senturia S D and Haritonidis J H 1988 Design and calibration of a microfabricated floating-element shear-stress sensor *IEEE Trans. Electron Devices* **35** 750–7
Shajii J, Ng K Y and Schmidt M A 1992 A microfabricated floating-element shear stress sensor using wafer-bonding technology *IEEE/ASME J. Microelectromech. Syst.* **1** 89–94
Stanton T E, Marshall D and Bryant C W 1920 On the condition at the boundary of a fluid in turbulent motion *Proc. R. Soc.* A **97** 413–34
Winter K G 1977 An outline of the techniques available for the measurement of skin friction in turbulent boundary layers *Prog. Aerospace Sci.* **18** 1–57